UTRECHT UNIVERSITY

DEBYE INSTITUTE FOR NANOMATERIALS SCIENCE
CONDENSED MATTER AND INTERFACES

INVESTIGATING THE ELECTRONIC STRUCTURE OF TWO-DIMESIONAL SEMICONDUCTOR NANOSTRUCTURES WITH HONEYCOMB GEOMETRY

December 13, 2019

Name:
Tomas Meerwijk
Student ID:
5731496

Supervisors:
L.C. Post, MSc
Dr. I. Swart
Prof. Dr. D.A.M. Vanmaekelbergh

Abstract

Two-dimensional semiconductor nanostructures with honeycomb geometry are promising material for opto-electronic devices due to their unique electronic structure. The combination of semiconductor material and the honeycomb geometry allows for the incorporation of Dirac cones and flatbands in semiconductor devices. A PbSe quantum dot superlattice and two different patterned InGaAs quantum wells have been produced. The electronic structure was investigated with scanning tunneling microscopy and spectroscopy (STM/STS) in ultra high vacuum. The quantum dot superlattice was produced in the presence of organic molecules. The superlattice was first characterized by atomic force microscopy (AFM) to check the stability of the sample. The AFM measurements indicated a stable surface, however STM measurements remained too unstable. Therefore, STS measurements have not be performed. The samples produced by lithography proved more stable. The electronic structure showed the presence of the S band and P flat band on the bridge site. A combination of muffin tin calculations and experimental results suggest that the physics originating from the geometry are repeated for every step of the quantum well.

Contents

Chapter 1

Introduction

The discovery of graphene has initiated the interest in nanostructures with a honeycomb geometry. Due to the two-dimensional honeycomb arrangement of the carbon atoms, the energy dispersion relation is linear in the K-point of the Brillouin zone. This linear dispersion relation causes the electron to behave as massless particles, which can be interesting for opto-electronic devices.[1] However, graphene is a semi-metal, which means it is always conductive. If a materials is always conductive, it is not possible to turn it on or off. Therefore two-dimensional semiconductor nanostructures with a honeycomb geometry are hypothesized to be suited to be incorporation into opto-electronic devices. By combining a two-dimensional semiconductor material and the honeycomb geometry, it is hypothesized to generate devices that can be switched on and off and have the physics as found in graphene.[2–5]

The goal of this thesis is to identify the graphene physics in a two-dimensional semiconductor nanostructure with a honeycomb geometry. Two different techniques will be used to obtain such a structure; oriented attachment of PbSe quantum dots and patterning of an InGaAs quantum well. The electronic structure is probed by scanning tunneling microscopy (STM) measurements. The outline of the thesis will be as follows.

First, a chapter will be used to discuss the theory. In this chapter the electronic structure of semiconductors will be discussed first. The second part of the chapter will contain a background information on oriented attachment and the lithography techniques that are used to pattern the quantum well. Lastly, atomic force microscopy (AFM) and STM will be discussed.

In the third chapter, the synthesis methods for the nanostructures will be discussed. First the synthesis method of the quantum dot superlattice will be discussed. Thereafter, the electron beam lithography method and the block co-polymer lithography method will be discussed consecutively.

The fourth chapter will be used to present the results. First the results of the quantum dot superlattice will be presented. AFM measurements have been performed to check the stability of the sample. STM measurements have been performed to obtain topography images of the lattice. The electronic structure of the quantum dot superlattice has not been investigated due to the instability of the sample. The next results are of the lithography samples. The electronic structure of the

unpatterned quantum well will be discussed as well as the effect of the geometry on the electronic structure of the quantum well.

In the last chapter a conclusion will be presented according to the obtained results. Also possibilities for improvement will be discussed.

Chapter 2

Theory

Semiconductor nanostructures are interesting due to the size dependence of the electronic structure. The size dependence comes into play when the size approaches the exciton Bohr radius.[6] In the following chapter the electronic properties of semiconductors will be discussed first. In that section, the bulk semiconductor will be discussed, followed by the quantum confinement effects in semiconductors structures where one dimension approaches the Bohr radius. Last, the properties of two-dimensional semiconductor structures with honeycomb geometry will be explained. The two-dimensional semiconductor structures with honeycomb geometry are produced by two techniques, oriented attachment of PbSe quantum dots and patterning of an InGaAs quantum well. The patterning of the quantum well has been achieved by electron beam lithography and block co-polymer lithography. Background on both techniques will be discussed in the second part. Measurements have been performed by atomic force microscopy and scanning tunneling microscopy. These two measurements techniques will be discussed in the final part of this chapter.

2.1 Electronic Properties of Semiconductors

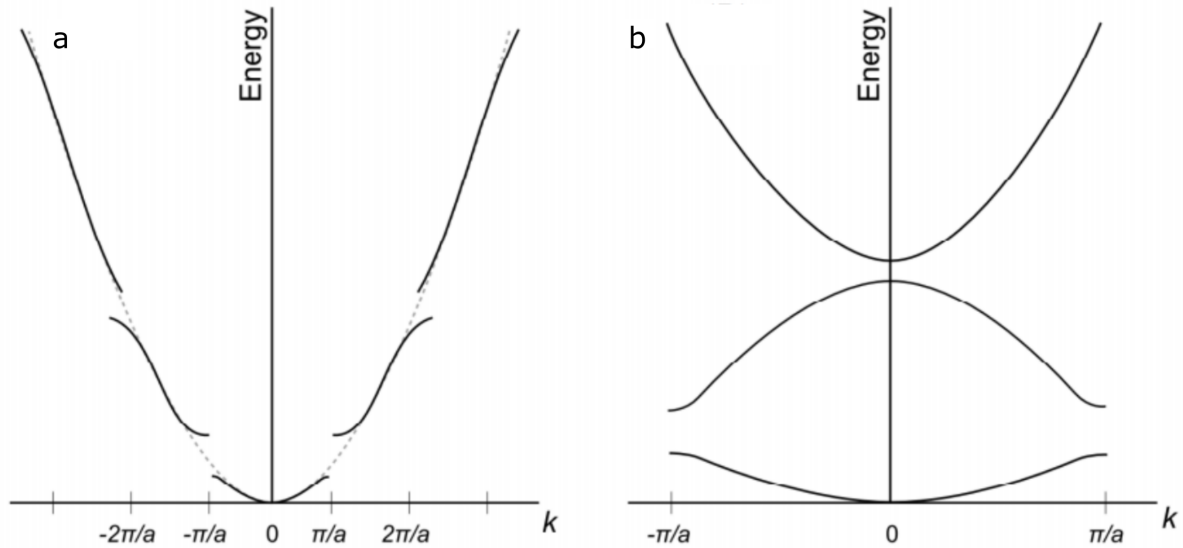### 2.1.1 Electrons in Bulk Semiconductor

Before discussing the behaviour of electrons in two-dimensional materials it is important to first examine the behaviour of electrons in bulk semiconductor. For simplicity, the derivation of the electronic structure of the electrons in bulk semiconductor will be performed in one dimension. The simplest model for describing electrons is by the free electron model, however electrons in a crystal are affected by the periodic potential imposed by the crystal lattice. Thus, the Hamiltonian not only contains a kinetic energy term, but also contains a potential energy term,[7] resulting in the equation:

$$\widehat{H} = \widehat{H}^0 + \widehat{V}(\vec{x}) = -\frac{\hbar^2}{2m}\frac{\partial^2}{\partial \vec{x}^2} + \widehat{V}(\vec{x}). \tag{2.1}$$

With $\widehat{H}^0$ being the kinetic energy operator of the electrons in the crystal and $\widehat{V}(\vec{x})$ the periodic potential operator as a result of the crystal lattice. Since $\widehat{V}(\vec{x})$ is periodic, i.e. $\widehat{V}(\vec{x}) = \widehat{V}(\vec{x}+\vec{a})$, with $\vec{a}$ the lattice vector, the result from the Schrödinger equation should be the same when translated by $\vec{a}$:

$$-\frac{\hbar^2}{2m}\frac{\partial^2 \psi(\vec{x}+\vec{a})}{\partial \vec{x}^2} + V(\vec{x})\psi(\vec{x}+\vec{a}) = E\psi(\vec{x}+\vec{a}). \tag{2.2}$$

The Bloch criterion states that $\psi(\vec{x})$ is periodic and therefore has the same eigenvalue as $\psi(\vec{x}+\vec{a})$. They can only differ by a phase vector.[8] The Bloch wave is a wavefunction satisfying this the Bloch criterion:

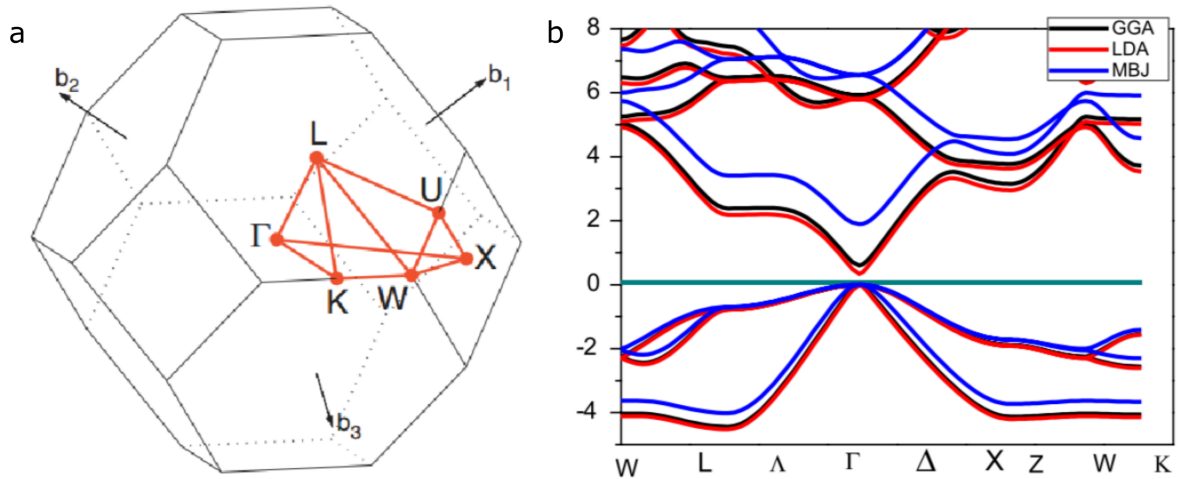
Figure 2.1: The dispersion relation in a one dimensional semiconductor material. At values of $k = \pi/a$, a discontinuity arises. a) The band structure before translation of the band and b) the band structure after translation of the bands to the first Brillouin zone.

6

$$\psi_{\text{Bloch},k}(\vec{x}) = e^{ik_x\vec{x}} \cdot u_k(\vec{x}) \tag{2.3}$$

where k_x is the wavevector in the x direction ($k = 2\pi/\lambda$) and $u_k(\vec{x})$ is a periodic function imposed by the crystal lattice. The first part of the Bloch wave, $e^{ik_x\vec{x}}$, is the phase of the wavefunction. The phase is modulated by the second part, $u_k(\vec{x})$, which describes the response of the valence electrons to the periodic potential of the crystal lattice. When the wavelength of the electrons is different from the periodicity of the crystal lattice the electrons behave like free electrons. However, when the wavelength approaches a, the electrons are scattered by the atoms in the crystal lattice, called Bragg reflection. This phenomenon results in a standing wave composed of two running Bloch waves, $\psi_{\text{Bloch},k}^+$ and $\psi_{\text{Bloch},k}^-$, with a wavelength equal to the crystal lattice. The running waves are moving in opposite direction and are translated by $a/2$. The resulting electron probability density is on the ions for $\psi_{\text{Bloch},k}^+$ and in between the ions for $\psi_{\text{Bloch},k}^-$, which lower and increase the overall energy respectively. A discontinuity arises in the dispersion relation due to the energy difference between between $\psi_{\text{Bloch},k}^+$ and $\psi_{\text{Bloch},k}^-$. This discontinuity results in forbidden energies for electrons, also called a band gap. The whole band structure can be displayed in a graph with values of k ranging from $-\pi/a$ to $+\pi/a$. This is because wavefunctions that differ by $n2\pi/a$ are equivalent. So, by adding or substracting $n2\pi/a$, every wavefunction can be translated to the regime between $k = -\pi/a$ and $k = +\pi/a$ (figure 2.1). This regime is called the first Brillouin zone.

So far the electronic structure is discussed using a one dimensional chain of atoms, but the real situation is a three-dimensional crystal. This means that there are multiple crystal lattices with possibly different periodicities present in the crystal and since Bragg reflection occurs when the

Figure 2.2: a) The first Brillouin zone of the cubic zincblende crystal structure. Adapted from ref.[9] b) The band structure of bulk CdSe with the zincblende crystal structure calculated with DFT. The calculations have been performed using the generalised gradient approximation (GGA), local density approximation (LDA) and the modified Becke-Johnson functional (MBJ). Adapted from ref.[10]

wavefunction has the same periodicity as the lattice, the band structure will become more complex. In three dimensions, Bragg reflection can occur at different points in k space. High symmetry points in the Brillouin zone are indicated with letters dependent on the crystal structure. The centre of the Brillouin zone ($k_{\tilde{x}} = 0, k_y = 0, k_z = 0$) is for every crystal structure the Γ point. The first Brillouin zone of the zincblende crystal structure and the band structure for bulk CdSe with the zincblende crystal structure is shown in figure 2.2.
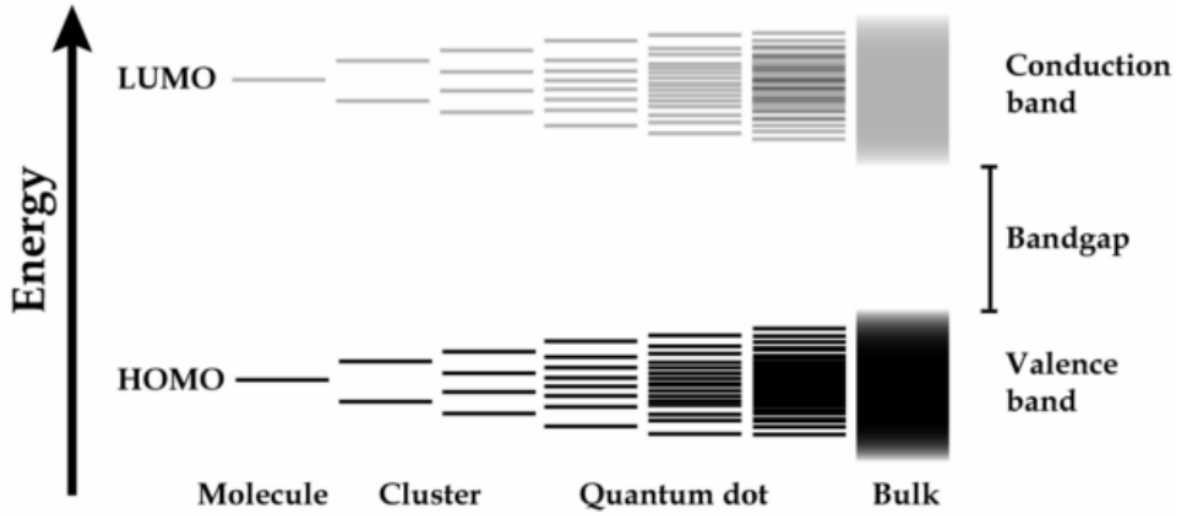
2.1.2   Electrons in Two-Dimensions

The previous section was about the electronic structure of a crystal with infinite sizes in each dimension. However, when one (or multiple) dimension of the crystal has a finite size, the electrons and holes are spatially confined in that dimension. When the size of the crystal in one (or multiple) dimension approaches the exciton Bohr radius, a phenomenon called quantum confinement occurs. citeKoole2014 The exciton Bohr radius is material specific, but is on the order of ten nanometers.[6] In the next section, quantum confinement will be explained via a bottom-up and top-down approach.

2.1.3   Quantum Confinement

Bottom-Up Approach

The bottom-up approach of explaining quantum confinement is by treating the nanocrystal as a molecule.[11] The basis of this approach is the linear combination of atomic orbitals (LCAO) approach. When two atoms form a diatomic molecule, the atomic orbitals form bonding and anti-bonding orbitals. The overall energy can be decreased when the electrons occupy the bonding orbital. By increasing the number of atoms in the molecule, the number of molecular orbitals increase centered around the bonding and anti-bonding molecular orbitals. When the number of atoms gets large enough, which is valid for large molecules, the bonding and anti-bonding orbitals become closely spaced. This results in the distinct energy levels becoming a continuum, also called bands. The band composed of the bonding orbitals is called the valence band (VB) and the band composed of the anti-bonding orbitals is called the conduction band (CB). The band gap is defined as the difference between the highest occupied molecular orbital (HOMO) and the lowest unoccupied molecular orbital (LUMO). When the size in which the electrons and holes are confined decreases in size, the band gap increases. For nanocrystals with one (or multiple) dimension approaching the exciton Bohr radius, the crystals is in between a molecule and an infinitely sized crystal. This has the effect that atomic orbitals start forming bands but at the top and bottom of the valence conduction band discrete energy levels occur. A graphical representation of the change of energy levels into bands is shown in figure 2.3.

Figure 2.3: A graphical representation of energy levels when going from a molecule to a cluster of atoms and from a cluster of atoms to bulk material. Adapted from ref.[12]

Top-Down Approach

Quantum confinement can also be explained via the top-down approach. With this approach, the Bloch wavefunction, that was derived for an infinitely sized crystal, is being multiplied by an envelope function:[12, 13]

$$\Psi_{\text{total}}(\vec{r}) = \psi_{\text{Bloch}}(\vec{r})\phi_{\text{env}}(\vec{r}). \tag{2.4}$$

The envelope function depends on the dimensions the charge carriers are confined in. The confinement effect only allows standing waves of the charge carriers to exist in the confined dimension. For quantum dots, spherical nanocrystals, the carriers are confined in all dimensions. This results in the envelope function containing all three dimensions. It is however more convenient to write the envelope function in terms of a radial and angular part:

$$\phi_{\text{env}}(\Theta, \Phi, r) = Y_l^m(\Theta, \Phi) R(r) \tag{2.5}$$

However, for nanocrystal in which confinement happens in one dimension, the envelope function consists of one dimension. In a crystal with a finite thickness, the electrons are free to move in the x and y directions, but are confined in the z direction. The envelope function is in the form:

$$\phi_{\text{env}}(z) = A\sin(k_z z). \tag{2.6}$$

with A a normalization term and k_z the wavevector in the vertical dimensions.
The value for the wavefunction has to be zero at the top and bottom of the semiconductor. This is

Figure 2.4: A graphical representation of the change in band structure when decreasing the size of the crystal. Left is the band structure for bulk material, moving to the right corresponds to a smaller crystal size. Adapted from ref[6]

true when $\sin(k_z z) = 0$ for $z = 0$ and $z = L_z$. From this, an expression for k_z can be derived:

$$k_z = \frac{\pi n}{L_z}. \tag{2.7}$$

Here n is a positive integer number and L_z is the size of the crystal in the z-direction. By inserting this expression for k_z into equation 2.6 and normalizing the function, an expression for the envelope function is obtained:

$$\phi_{\text{env}}(z) = \sqrt{\frac{2}{L_z}}\sin(\frac{n\pi z}{L_z}). \tag{2.8}$$

The eigenvalue of the equation can be determined by letting the Hamiltonian operator of equation 2.1 work on the envelope wavefunction, which results in:

$$E_n^{\text{conf}}(L_z) = \frac{\hbar^2 n_z^2 \pi^2}{2m_{e,h}^* L_z^2}. \tag{2.9}$$

In this result, m^* is the effective mass of either the electron or the hole. The band gap of the two-dimensional semiconductor is a sum of the original band gap (i.e. the band gap of the bulk material) and the confinement energies of both the electrons and holes. This results in the function for the total band gap:

$$E_g^{tot}(L_z) = E_g^0 + E_n^{\text{conf}}(L_z) = E_g^0 + \frac{\hbar^2 n_z^2 \pi^2}{2m_e^* L_z^2} + \frac{\hbar^2 n_z^2 \pi^2}{2m_h^* L_z^2}. \tag{2.10}$$

By treating the hole and electron energy levels independently, the assumption is made that it is not longer possible to form a bound exciton due to the weaker coulomb interaction between the electron and the hole. This assumption can be made when the size of the confined dimensions is smaller than the exciton Bohr radius. It might seem counter intuitive that the coulomb interaction is smaller, since the hole and the electron are confined a smaller region than for the bulk crystal. However, due to the confinement, the kinetic energy of both the electron and the hole is much larger than the Coulomb interaction between them. Which means that they become uncorrelated and can therefore be treated separately. It can also be noted that the band gap is inversely proportional to the thickness: $E_g \propto L_z^{-2}$. This can be observed in nanoplatelets with varying vertical dimensions.[14] A graphical representation of the change in spacing of the energy levels when decreasing the crystal size can be observed in figure 2.4.

2.1.4 Density of States

The density of states is a measure of the amount of states per unit energy. This can be calculated as follows. For every allowed state an electron can occupy, the motion of the electrons is described by k_x and k_y. A grid can be constructed with the wavevectors k_x and k_y as the two axes. The wavevectors form a square grid with $\pi/L_{x,y}$ as the spacing between allowed states.[15] The area of a single grid point, or state, is:

$$A_{state} = \frac{\pi}{L_x}\frac{\pi}{L_y} = \frac{\pi^2}{A}. \tag{2.11}$$

with L_x and L_y being the size of the material in the x and y dimension in real space and A being the area of the material in real space. The number of available states for a certain magnitude for $k\left(= \sqrt{k_x^2 + k_y^2}\right)$ is a ring with radius k and thickness dk. The center of the ring lies at the origin $k_x = k_y = 0$ as the centre. The area of this ring is given by $2\pi k dk$. The number of states, $g(k)dk$, is:
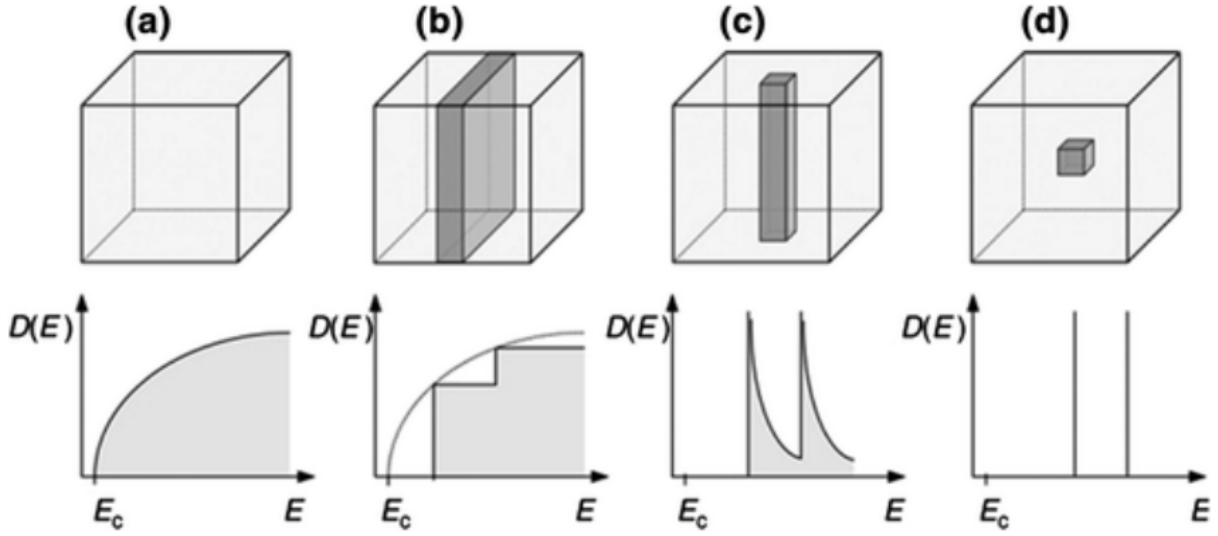
$$g(k)dk = \frac{A_{ring}}{A_{state}} = 2 * \frac{1}{4} \cdot 2\pi k dk \cdot \frac{A}{\pi^2} \tag{2.12}$$

The factor of 2 accounts for the fact that two electrons with opposite spin can occupy the same state. The factor of 1/4 accounts for the fact that only positive k_x and k_y are allowed. The number of available states can be written in terms of energy by using the relation between k and E from the formula for the energy of a free electron:

$$g(E)dE = \frac{A}{\pi}k dk = \frac{A}{\pi} \cdot \left(\frac{2m^*E}{\hbar^2}\right)^{1/2} \cdot \frac{m^*}{\hbar(2m^*E)^{1/2}}dE = \frac{Am^*}{\pi\hbar^2}dE \tag{2.13}$$

From this, the density of states per area can be obtained:

$$D(E) = \frac{g(E)}{A} = \frac{m^*}{\pi\hbar^2} \tag{2.14}$$

Figure 2.5: A graphical representation of the density of states when quantum confinement occurs in 0D (bulk), 1D(quantum well), 2D (rod) and 3D (quantum dot). Adapted from ref[16]

The result for the density of states is independent of the energy. This means that the density of states is a constant function. The real scenario is a stepwise increase in the density of states. This is because a two dimensional material in real life is not perfectly two dimensional, but has a finite thickness. Therefore, there are distinct values that are allowed for k_z. This results in an extra term in the density of states:
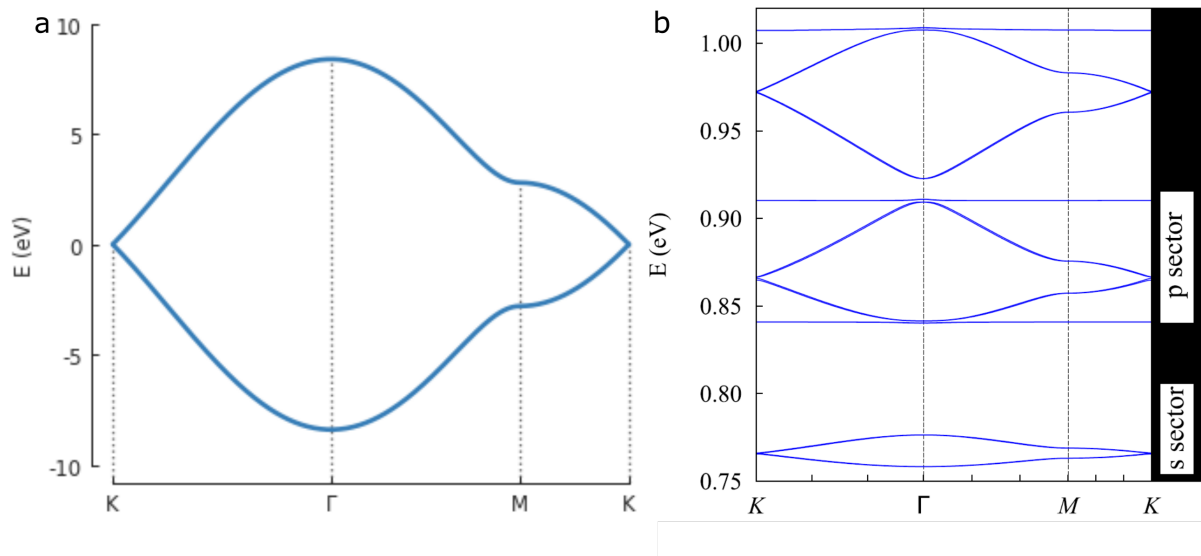
$$D(E) = \frac{m^*}{\pi\hbar^2} * k_z. \tag{2.15}$$

In the derivation for the quantum confinement effect k_z is shown to take discrete values of $n\pi/L_z$. So the density of states increases stepwise each energy level.[17] Figure 2.5 is a graphical representation of the effect of quantum confinement on the density of states.

2.1.5 Electrons in Two-Dimensions with a Honeycomb Geometry

The next step is to take the two-dimensional material and impose a periodic potential on the electrons. By choosing the periodic potential to have a triangular geometry, the electrons are forced to move in a honeycomb pattern as is well known in graphene. This combines the electronic structure of a two-dimensional semiconductor with the electronic structure of graphene. Graphene is well known for the linear dispersion at the K-point in the $E(k)$ diagram. A linear dispersion in the $E(k)$ diagram means that the electron have an effective mass of zero. This is because the effective mass is defined by:[7]

$$m^* = \frac{\partial^2 k}{\partial E^2}. \tag{2.16}$$

An effective mass of zero means that the electrons will behave as photons. Therefore the charge

Figure 2.6: a) A tight binding calculation for the band structure of graphene. b) A tight binding calculation for an InAs honeycomb superlattice with a periodicity of 24.5 nm. Adapted from ref.[19]

carriers can move quickly through the materials and result in a high mobility.

Incorporating the graphene physics into opto-electronic devices can increase the versatility. However, opto-electronic devices require the ability to be switched on and off. Since graphene is a semi-metal, it is not possible to turn off. Another disadvantage is that properties of graphene are not tunable because it solely consists of carbon atoms. By having the ability to choose between several elements, the properties of the material can be accurately tuned. Therefore experimental and theoretical research is being performed on two-dimensional semiconductor nanostructures with a honeycomb geometry. Calculations have shown that Dirac cones and flatbands are formed in the conduction band of two-dimensional semiconductor superlattices with honeycomb geometry.[18] The first Dirac cone is formed by the 1S envelope function and at higher energies the 1P envelope function forms the P bands with a Dirac cone and two flat bands.[19] This combination of semiconductor and honeycomb geometry utilizes the tunability of the semiconductor and the graphene physics of the honeycomb geometry.

2.2   Fabrication Methods

There are two main methods to obtain a semiconductor honeycomb superlattice, a bottom-up method and a top-down method. The bottom-up method is by self-orientation of quantum dots. The top-down method is by using lithography to etch pores into a two-dimensional semiconductor. The background of both methods will be discussed in this section.

2.2.1 Bottom-Up

Much research has been performed towards the self assembly of nanocrystals with varying compositions. It has been shown that isotropic nanocrystals can form into anisotropic single crystalline nanocrystals like wires, platelets and sheets.[14,20–23] Later, it has also been shown that anisotropic attachment of quantum dots can also result in a quantum dot superlattices.[24] The quantum dots superlattice have been shown to be formed by truncated cubic PbSe quantum dots.[25] By oriented attachment of these quantum dots, a superlattice can be obtained with a honeycomb or square geometry. Interestingly, both geometries are obtained when the 100 facets of the quantum dots attach.[26,27] A typical synthesis method involves dropcasting a quantum dot solution onto a liquid substrate. This liquid substrate is often a viscous liquid, such as ethylene glycol. After dropcasting there is a waiting period. The quantum dots orient themselves and eventually, if the conditions are right, attach. There are many variables that can be altered. Different liquid substrates can be used, extra ligands can be added onto the liquid substrate. The vapour pressure of the solvent can be increased by placing a beaker over the dish containing the liquid substrate. Another important factor is the temperature. If the temperature is too low, the quantum dots are likely not to attach. If the temperature is too high, the quantum dots can melt.[28]

2.2.2 Top-Down

The top-down method involves etching a geometry into a material. The geometry of the samples that are investigated in this thesis are obtained by accurately focusing an electron beam onto a polymer material and by the self assembly of two types of polymers. Henceforth, these methods will be named electron beam lithography (EBL) and block co-polymer lithography (BCPL).

Electron beam lithography utilizes the interaction of a material (resist) with the electrons from the electron beam. The material can be either a positive or a negative resist. By applying an electron beam dose onto the resist, the structure of the resist changes. A resist developer is a solvent that is used to wash away either the exposed resist or the unexposed resist. If a positive resist is exposed, it become soluble in the resist developer. Whereas, if a negative resist is exposed it becomes less soluble in the resist developer.[29] Due to higher resolution capabilities, positive resists are used more often than negative resists. An example of a positive resist is polymethylmethacrylate (PMMA). By applying an electron beam dose, the structure changes and it can be washed off by a methyl-isobutylketone and isopropanol mixture as the resist developer.

Block co-polymer lithography utilizes the interaction between two chemically different covalently bound polymers to acquire the desired geometry. A predetermined amount is spincoated on the material that is to be etched. By increasing the temperature, the polymers start to aggregate. Domains are formed consisting of the same polymers which are linked to domains consisting of the other polymers. Examples of combinations of polymers are polystyrene (PS) and PMMA, PS and polybutadiene (PB) and PS and polyethyleneoxide (PEO).[30–32] By tuning the chain lengths of the polymers and the types of

polymers that are used, different geometries can be obtained. To etch the geometry in the underlying material, one of the polymer must be removed. Ozone can be used to remove one of the polymers. Alternatively, one of the polymers can be stained with, for instance, osmium. Staining one of the polymers ensures that the polymer is not removed during the following etching step.[30]

Electron beam lithography has the advantage that the location of the pores is accurately determined by the location of the electron beam. This can result in pores that are evenly spaced and a lattice that has a single orientation of the geometry. A downside is the speed at which the sample is prepared, each location of the pore has to be exposed individually. Therefore, the smaller the features, the longer the preparation time while maintaining the same area size. Block co-polymer lithography is less ordered, due to the self assembly of polymers. The flexibility and self assembly of the polymers cause the lattice to contain different orientations of the geometry. The upside of this technique is the fact that a sample is relatively quickly prepared. The polymer material is spincoated on the material that is to be etched. After heating, the polymer that is to be removed can be rinsed off and the etching procedure can start.
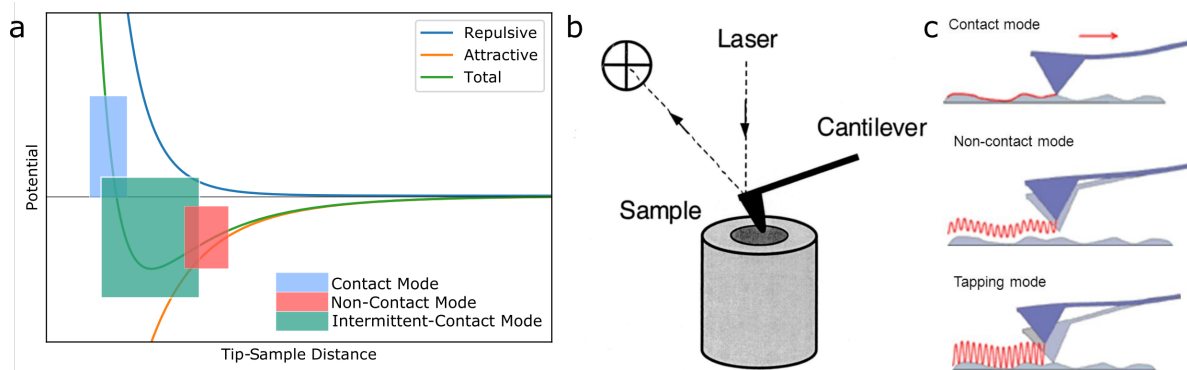
In both methods, the geometry must be etched into the underlying material. That is often achieved by reactive ion etching (RIE). A gas is inserted into the preparation chamber and an electromagnetic field is applied to the sample. This electromagnetic field ionizes the molecules, thereby generating a plasma. The electric field accelerates the ions towards the sample and removes the material, thereby etching the geometry into the underlying material. Another type of etching is inductively coupled plasma (ICP) etching. This technique is similar to RIE, the difference is that a magnetic field induces the electric field. This technique results in a high plasma density.[33] Many different types of gas molecules can be used, but often has the molecular formula AX_n. The first element (A) can be i.e. boron, carbon, sulfur, silicon, and the second element (X) is a halide or hydrogen or a combination of both.[34]

2.3   Experimental Setup

To characterize the structural and electronic properties, atomic force microscopy (AFM) and scanning tunneling microscopy and spectroscopy (STM/STS) measurements were performed on the nanostructures. The AFM measurements were performed in ambient conditions. The STM measurements on the quantum dot superlattice were performed at 80K and the STM measurements on the InGaAs superlattice were performed and at 4.5K. Both STM measurements were performed in ultra high vacuum ($P < 10^{-10}$ mbar) conditions. The theoretical background of both techniques will be briefly discussed.

2.3.1   Atomic Force Microscopy

When performing measurements, the AFM measures the interaction between the tip and the sample which consists of attractive and repulsive interactions.[35] The interactions mainly consists of the

Figure 2.7: a) The force-distance curve of the Lennard-Jones potential with regions indicated corresponding to the operating modes of the AFM. b) A graphical representation of the set-up of an AFM adapted from ref.[37] c) A graphical representation of the movement of the tip for the different operating modes of the AFM adapted from ref[38]

.

attractive Van der Waals interaction and the Pauli repulsion.[36] The Van Der Waals interaction is an attractive interaction which originates from dipole-dipole interactions. Pauli repulsion is the repulsion of electrons when they get too close to each other. The combination of these interactions can be described by the Lennard-Jones potential:

$$V_{LJ} = \epsilon \left[\left(\frac{\sigma}{r} \right)^{12} - 2 \left(\frac{\sigma}{r} \right)^{6} \right] \tag{2.17}$$

With ϵ being the depth of the potential well. r the distance between the tip and the sample and σ the point on r where $V_{LJ} = 0$.

AFM can be used for obtaining topographical images, but also non-topographical images. For the purposes of this master thesis only topographical images are obtained. Other applications will therefore not be discussed. AFM measurements can be performed in three different modes, contact mode, non-contact mode and tapping mode (intermittent-contact mode). These different modes correspond to three regions in the Lennard-Jones potential. A graphical representation of the Lennard-Jones potential and the individual interactions is shown in figure 2.7a. During the measurements a laser is pointed on top of the cantilever. The laser is reflected onto a 4-segment photodiode which converts the signal from the laser to the height difference (Figure 2.7b). The measurements in this thesis have solely been performed in tapping mode, therefore this mode will be discussed.

Tapping mode, or intermittent contact mode, is an operating mode for the AFM in which the tip of the AFM is oscillating over the sample at a certain frequency, this oscillation frequency is dependent on the cantilever.[39] The oscillation frequency is dependent on the distance to the sample. If, during scanning, the tip encounters an increase in height, i.e. the tip - sample distance gets smaller, the tip starts oscillating at a lower frequency. In intermittent contact mode the tip makes contact with the sample during every oscillation (figure 2.7c). The advantage of this is that contamination, like an oxidation layer, can be penetrated and therefore a more correct image of the surface can be obtained.

Another advantage is that the risk of tip damage has decreased compared to contact mode, in which the tip follows the surface, while still high accuracy can be attained.[40] Due to the mentioned advantages, the AFM measurements during this master project are performed in intermittent contact mode.

For all SPM methods, the state of the tip will highly affect the images it produces.[41] The obtained images are a convolution of the shape of the tip and the sample. An important property of the tip is the curvature radius, which directly influences the maximum achievable resolution. A distinction is made between three different types of tips depending on their curvature radius: normal tips, with a curvature radius of about 30 nm; super tips, with a curvature radius of about 20 nm; and the super sharp tips, with a curvature radius of less than 6 nm. During measurements, damaging of tips during measurements is inevitable. A common defect is a dull tip, this means it has an increased curvature radius. This translates in a decrease in resolution. Another common defect is an irregularly shaped tip. An irregular shape can include any shape that is not spherical. It can also happen that the tip is split into multiple tip, with the consequence that the measurements are effectively performed with multiple tips. These defects are directly visible in the height profile. A deformed tip can induce recurring irregular shapes of an object, or have the result that an object is measured multiple times.

2.3.2 Scanning Tunneling Microscopy

STM is used to obtain the topographical and electronic properties of an object and therefore, as opposed to AFM, requires a conductive sample. The physical basis of this technique is the tunneling phenomenon of electrons emanating from the wavelike character of the electrons. During the measurement, the tip of the STM raster scans the surface at a certain bias voltage and measures the current (figure 2.8. The current is a function of the local density of states of the tip, the local density of states of the sample and a factor which is dependent on the distance between the tip and the sample[42–44] :

$$I = A \int_0^{eV} T(E, V_b, z) \rho_s(E) \rho_t(E - eV_b) dE. \tag{2.18}$$

Here, ρ_t and ρ_s are the local density of states of the tip and sample, respectively. The tip-sample distance is given by z with z=0 at the sample and T is the height dependent transmission coefficient:
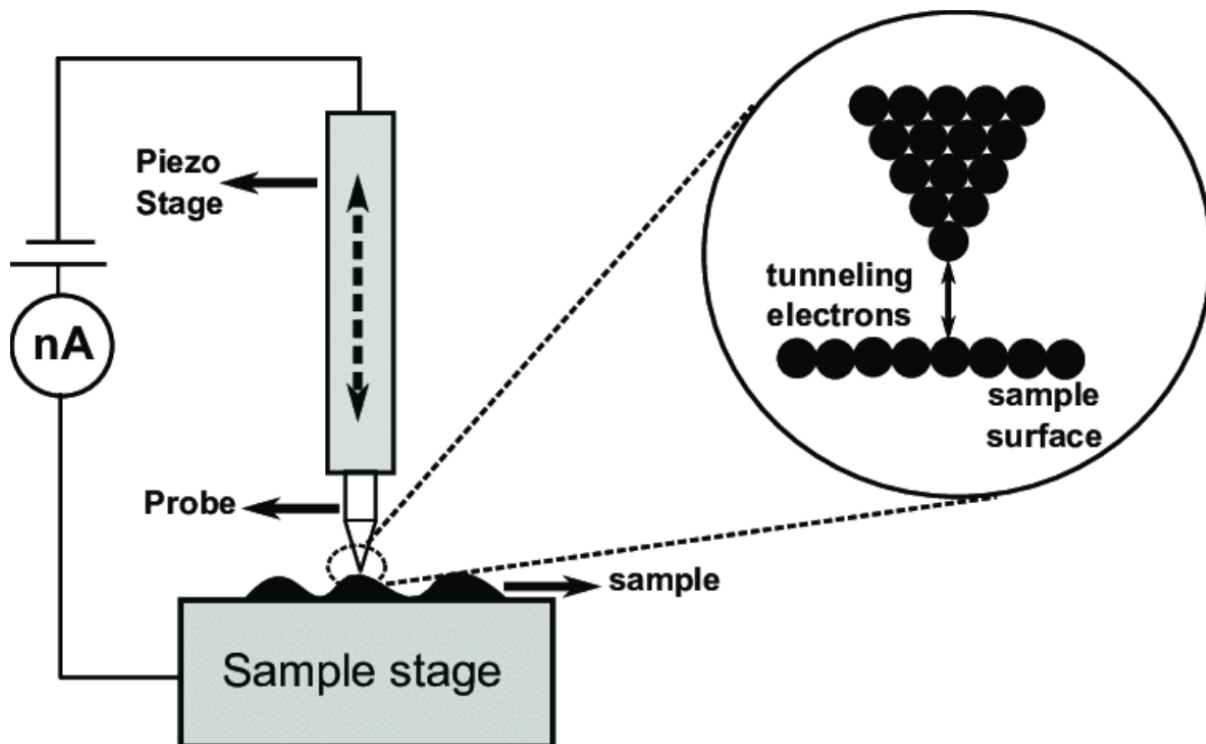
$$T = \exp(-2\kappa z). \tag{2.19}$$

where κ is a material specific decay constant.

The exponential dependence of the tunneling current on the tip-sample distance allows for high resolution of the topographical images. It is however possible to probe the electron structure by performing differential conductance spectra at constant height. The differential conductance can be derived from equation 2.18:

$$\frac{dI}{d(eV_b)} = A \left\{ T(eV_b, V_b, z) \rho_s(eV_b) \rho_t(0) + \int_0^{eV_b} \rho_s(E) \frac{d[T(E, V_b, z) \rho_t(E - eV_b)]}{d(eV_b)} dE \right\} \tag{2.20}$$

Figure 2.8: A graphical representation of the set-up of an STM. Adapted from ref[46]

with the density of states is given by the first term and the background by the second term. By assuming that the transmission coefficient and the density of states of the tip vary minimally with the bias voltage, the local density of states of the sample can be directly determined from the differential conductance measurements:

$$\frac{dI}{dV_b} \propto \text{LDOS}(eV_b, \text{sample}). \tag{2.21}$$

To validate the assumption that the density of states of the tip is invariant of the applied bias voltage, a metallic tip is used during measurements. This is because a metallic tip is an excellent conductor, but more importantly, it has a relatively flat density of states.[45]
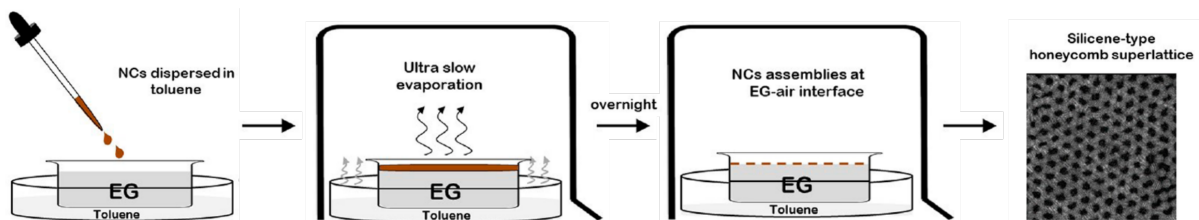
Chapter 3

Synthesis Methods

In the next chapter, the methods will be discussed that are used to obtain the samples measured in this thesis. The first method is the bottom-up approach, where PbSe quantum dots are synthesized and dropcasted onto a liquid substrate. By oriented attachment these quantum dots form a superlattice. The second approach is the top-down approach. With this approach, lithography is used to etch a triangular arrangement of pores into a quantum well. This results in a quantum well with a honeycomb geometry. The sample that was obtained by electron beam lithography will be discussed first, followed by the sample that was obtained by block co-polymer lithography.

3.1   Bottom-up

The synthesis of a quantum dot superlattice[47] is performed by dropcasting a dispersion of 7 nm PbSe quantum dots in toluene onto a ethylene glycol (EG). This is placed in a petridish with additional toluene and covered with a beaker. A graphical representation is given in figure 3.1. This caused ultraslow evaporation of the solvent (~16 hours) and can result in the formation of a long range superlattice with honeycomb geometry. Even though this yielded long range patches of superlattice with honeycomb geometry, there are also patches with square geometry. The 16 hour evaporation period was overnight at 22 °C, followed by a period of 15 minutes at 50 °C. The superlattice was stamped on HOPG and put in vacuum to dry. After leaving it overnight, the HOPG with the lattice was placed in a solution of CdI_2 in Methanol for a few minutes, to replace the surface passivating ligands with Cd. Prior to STM measurements, the sample was annealed at 100 °C for a few hours.

Figure 3.1: A graphical representation of the synthesis method of the PbSe honeycomb superlattice adapted from ref.[47]
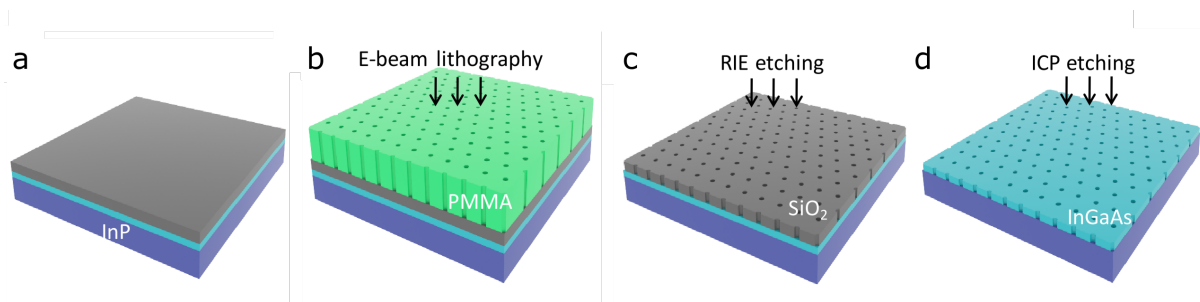
3.2   Top-down

The top-down approach is performed by etching holes into an InGaAs quantum well. One sample is produced by EBL and another is produced by BCPL. The preparation procedures will be discussed here.

First, both sample were grown. A 10 nm thick InGaAs quantum well was grown on an InP layer using molecular beam epitaxy (MBE). MBE is a method in which a material is heated to the point where it starts sublimating. The gaseous material then condenses onto the substrate.[48] A 16 nm silica layer is grown on top of the quantum well (figure 3.2a) by plasma enhanced chemical vapor deposition (PECVD). Subsequently the sample was dried at 180°C for 10 minutes.

3.2.1   Electron Beam Lithography

On top of the silica layer, 50 nm of a diluted PMMA 950K 4% resist was spincoated. Subsequently, the sample was annealed at 80°C for 1 minute followed by a bake out at 180°C for 10 minutes. On the resist, spots in a triangular pattern were exposed (figure 3.2b) by the electron beam with a current of 200 pA, an accelerating voltage of 100 kV and an electron beam dose of 10000 $\mu C/cm^2$. The exposed resist was removed by development in a 1:2 methyl-isobutyl ketone:isopropanol solution for 60 seconds. The

Figure 3.2: A graphical representation of the preperation method of the patterned InGaAs lithography sample. Adapted from ref.[49]

development was terminated by rinsing the sample in isopropanol for at least 30 seconds, followed by drying under a low N_2 flow.

The next step was to etch the triangular pattern into the SiO_2 layer (figure 3.2c). This was achieved by reactive ion etching with a mixture of CHF_3 and CF_4. The sample was etched for 40 seconds with a power of 300W, the pressure in the chamber was set to 10 mTorr. After 40 seconds, the SiO_2 at the location of the pores is expected to be entirely removed. The sample is placed in a SVC bath at 70 °C for 2 minutes, followed by an acetone bath for 2 minutes and lastly an isopropanol bath for 2 minutes to remove the remaining PMMA resist. The sample was further rinsed with isopropanol and a low N_2 flow.

The last step is to etch the triangular pattern into the InGaAs QW (figure 3.2d). The etching step is performed using BCl_3 based inductively coupled plasma etching with a power of 200 W and reactive ion etching with a power of 50 W. The InGaAs in the pores are removed by etching the sample for 40 seconds in a chamber with a pressure of 2 mTorr. The remaining SiO_2 mask was removed by 1% HF etching for 1 minute.

Before transferring the sample to the STM, an arsenic layer was grown on the sample. This was to protect the sample for oxidation. Before performing the STM measurements, the arsenic layer was removed by annealing. The annealing procedure was as follows. The temperature of the sample was increased to 350 °C in one hour. The sample was kept at 380 °C for an hour an left to cool down to room temperature before placing the sample in the microscope head.

3.2.2   Block Co-polymer Lithography

The exact method for this sample is not yet communicated, a general description will be discussed. The geometry on the BCPL sample can be obtained by the self assembly of PS and PB. The PS formed the lattice and PB occupied the location of the pores. PB is removed by ozone treatment and the PS remained. The next steps are to etch the pores in the silica layer and subsequently in the InGaAs layer. These steps are the same as described for the EBL sample.

As for the EBL sample, an arsenic layer was grown on the sample to protect it from oxidation. This layer was removed before the STM measurements by annealing. The annealing procedure was

as follows. The temperature of the sample was increased to 300 °C in 2 hours and kept at 300 °C for 5 hours. The sample was left to cool to room temperature overnight before inserting it into the microscope head. It is worth noting that this annealing procedure is significantly longer and at a significantly lower temperature than for the previous sample.
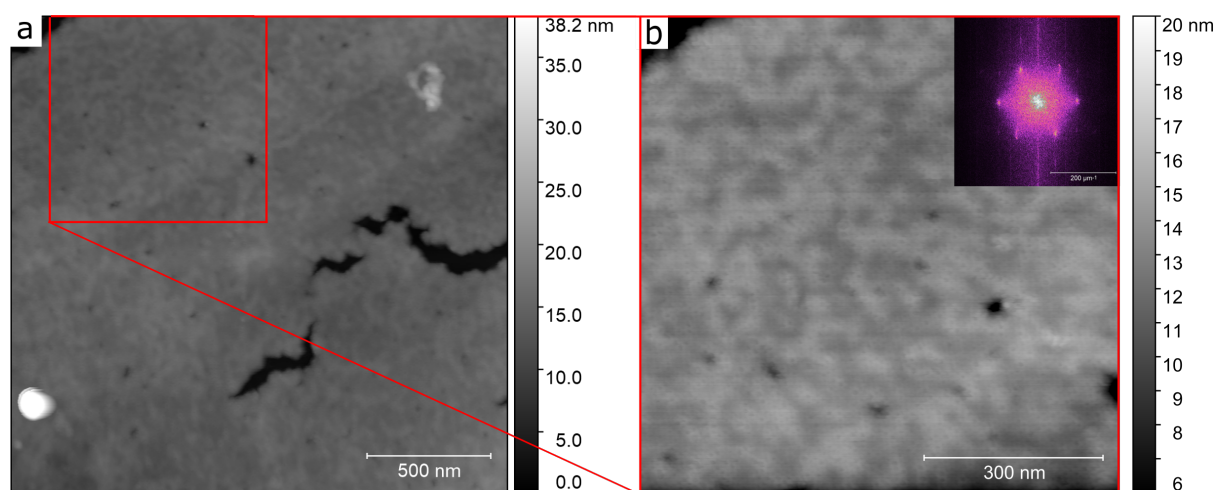
Chapter 4

Results & Discussion

In this chapter the results will be discussed. The PbSe superlattice sample was characterized by AFM to check the stability of the sample. Subsequently, STM measurements were performed as an attempt to investigate the electronic structure. The samples produced by electron beam lithography and block co-polymer lithography, are both characterized by STM. Topography images of the samples are obtained as well as dI/dV spectra.
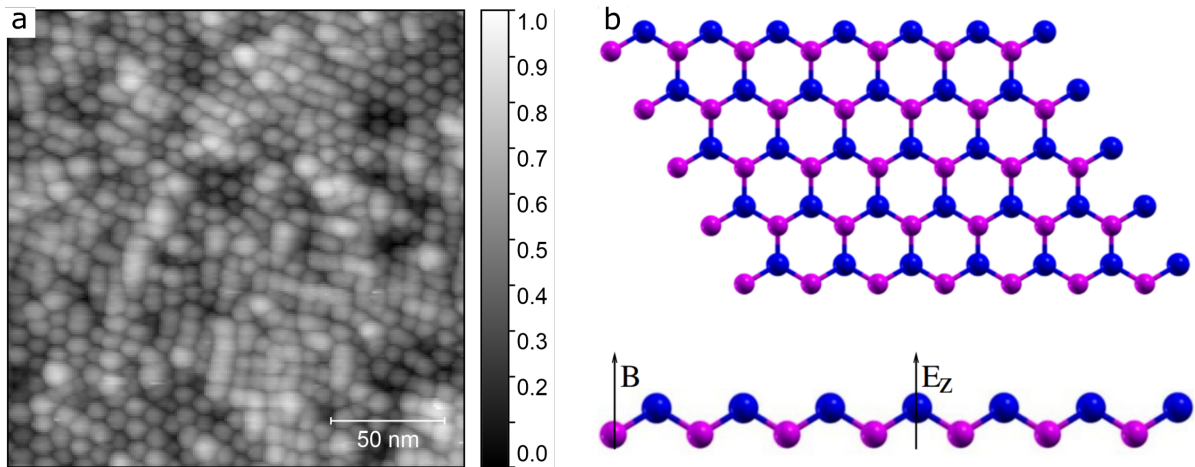
4.1 PbSe Quantum Dot Superlattice

The quantum dot superlattice is synthesized with a wet chemical method, therefore it is inevitable that the chemicals that are present during the synthesis are also present on the sample. Ligands are attached to the quantum dots and are dispersed in toluene and dropcasted onto ethylene glycol. All these hydrocarbons are likely to be present on the sample when it is inserted into the vacuum and placed in the microscope. Consequently, it is likely that the molecules stick to the tip of the AFM or STM and interfere with the measurements. Therefore, prior to performing STM measurement, samples were produced with different cleaning steps to check for the optimal method to produce clean samples on which stable measurements can be performed. AFM measurements in ambient conditions were performed to check the stability of the measurements. Ambient AFM measurements are significantly faster and easier to perform compared to STM measurements in ultra high vacuum. If the AFM measurements are stable and clean, then the synthesis and preparation method can be used to produce samples for the STM.

Figure 4.1a shows an image of the superlattice sample as measured in the AFM. The crack in the middle right part of the picture is likely caused by the stamping process. Figure 4.1b shows a zoom-in, darker spots can be observed. These spots might be the pores between the quantum dots. However, it is not possible to determine the geometry by eye, therefore a Fourier transform is constructed. The inset shows the Fourier transform of the zoom-in. A Fourier transform of the image contains peaks in reciprocal space corresponding to spatial frequencies present in the real space image. The Fourier transform contains peaks in a sixfold symmetry, these are likely caused by the sixfold symmetric honeycomb geometry. The frequency of the peaks corresponds to a periodicity of 8 nm, which corresponds to the distance between the triangular pattern of the holes of the honeycomb superlattice. Due to the large amount of stable measurements, the preparation method was accepted

Figure 4.1: a) An AFM topography image of the PbSe superlattice. b) A zoom-in of the larger scan, the inset is the Fourier transform.

Figure 4.2: a) An STM topography image of the PbSe superlattice. b) A graphical representation of the silicene type honeycomb superlattice adapted from ref.[50] The blue and the purple dots represent the inequivalent locations of the quantum dots.

as a method for preparing clean honeycomb superlattice sample. Therefore measurements were continued on new samples in the STM.

However promising the results of the AFM measurents, it proved difficult to perform stable STM measurements. It seemed that after passivating the superlattice with Cd and annealing the superlattice, there were still ligands and/or solvent molecules remaining on the sample. It was possible to obtain a small number of topographical images of the superlattice. Figure 4.2a shows the PbSe superlattice with in the top right and bottom left a triangular lattice. A triangular geometry is observed instead of a honeycomb, because of the silicene type lattice. This lattice is buckled and the quantum dots pointing upwards are in a triangular pattern (figure 4.2b). Incorporating the tip broadening results in the quantum dots appearing to be directly next to each other in a triangular pattern. During the measurements the tip swiftly degraded, this is likely due to the presence of ligands and solvent molecules. Even though it was possible to obtain topographical images, the spectroscopy measurements did not succeed and are therefore not presented in this thesis.
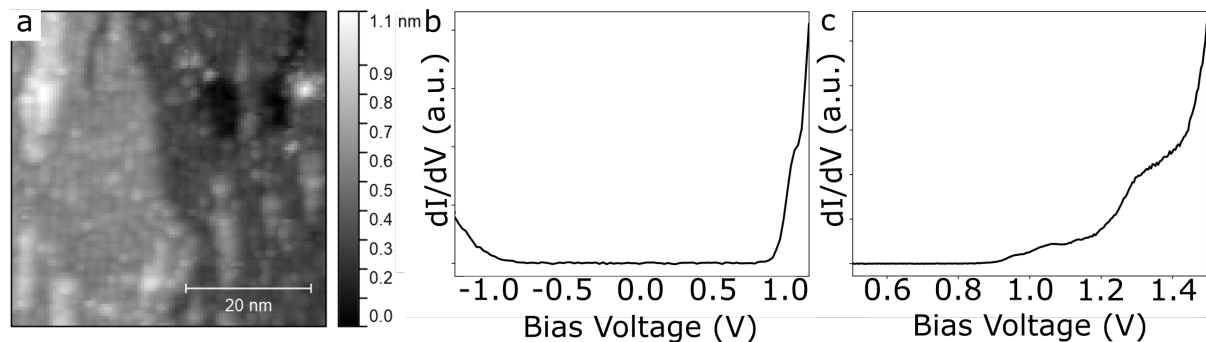
4.2 InGaAs Quantum Well

In this section, the results will be discussed of the samples that are produced by lithography. First, the effect of the lithography procedures on quantum well behaviour will be investigated. To investigate this, an area that is not perforated will be measured. After the investigation of the unperforated quantum well, the perforated quantum well will be investigated. For both investigations, the result from the EBL sample will first be discussed followed by the results from the BCPL sample. Earlier experiments on the quantum well before etching of the pores have shown that the InGaAs quantum well has a thickness of 10 nm and a band gap of 0.9 eV.[51]

4.2.1 Investigation of the Quantum Well Behaviour
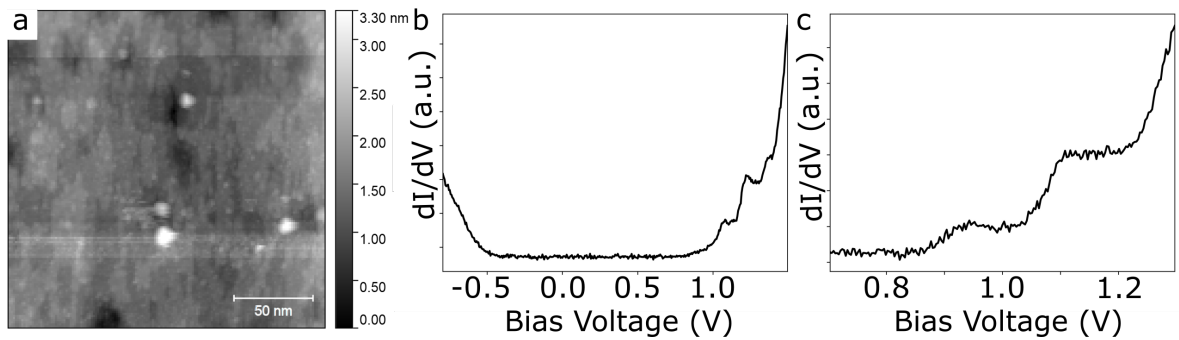
4.2.1.1 Electron Beam Lithography

A typical image of the unperforated quantum well is shown in figure 4.3). Figure 4.3b shows a dI/dV spectrum on the bare quantum well. The dI/dV spectra show that the valence band starts at -0.8eV and the conduction band starts at +0.9eV, this corresponds to a band gap of 1.7eV. This differs significantly with the earlier established band gap of 0.9eV. The perforated may have caused a reduction in the quantum well thickness, thereby causing an increase in the band gap. However, a two fold increase in the band gap means a thickness of 2.8 nm, since the band gap is proportional to $1/d^2$. It is unlikely that the lithography procedure has removed three quarters of the quantum well. It has been shown that a quantum well can have dead layers, meaning that parts of the top and/or bottom don't contribute to the quantum well. Thereby effectively reducing the thickness.[52,53] This might have been caused by the patterning, or by annealing. As will be shown later, the BCPL sample was annealed differently and the band gap was closer to the original band gap. The InP, on top of which the InGaAs quantum well was grown, was p-doped with beryllium. The annealing procedure was likely to have caused the beryllium dopants to migrate into the InGaAs quantum well and towards the surface. Eventhough doping solely alters the position of the Fermi level, it does not alter the size the band gap. This suggests that the presence of dopants increases the dead layer thickness and thereby increasing the size of the band gap. Despite the altered band gap, figure 4.3c shows steps in the conduction band, with the first step starting at +0.9V and the second step starting at 1.2V, thereby confirming that the quantum well behaviour is present.

Figure 4.3: a) A typical image of an unperforated part of the quantum well on the EBL sample. b) A full band gap dI/dV spectrum showing the first step. c) A zoom-in on the first and second step

4.2.1.2 Block Co-Polymer Lithography

Figure 4.4a shows a location where no pores were etched into the quantum well. The dI/dV spectra show (figure 4.4b) that the valence band starts at -0.4eV and the conduction band starts at +0.8eV, which corresponds to a band gap of 1.2eV. Unlike the EBL sample this corresponds well to the band gap measurement in earlier experiments. The difference in band gap is likely due to the different
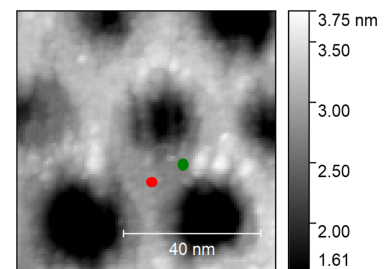
Figure 4.4: a) A typical image of the unperforated quantum well on the BCP sample. b) A full band gap dI/dV spectrum showing the first and second step. c) A zoom-in on the first and second step

annealing temperature. The annealing temperature was lower, which causes the dopants to migrate less than at higher temperatures. Figure 4.4c clearly shows the steps from the quantum well with the first step starting at 0.85V and the second step starting at 1.05V. This is a confirmation that the quantum well behaviour is still intact.

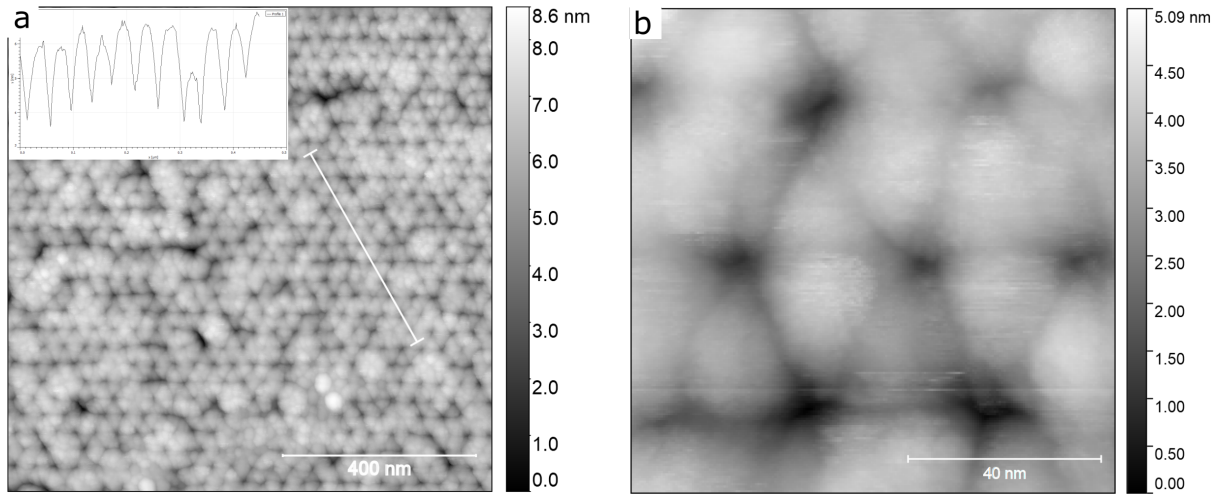### 4.2.2 Investigation of the Perforated Quantum Well

The perforated quantum well contains two main locations of interest, the "atomic site" and the "bridge site". The atomic site corresponds to the site in between three pores and the bridge site corresponds to the location in between the atomic sites. In figure 4.5 the two locations are indicated, red is the atomic site and green is the bridge site.

Figure 4.5: The location of the atomic site, indicated in red, and the location of the bridge site, indicated in green.

4.2.3 Electron Beam Lithography

After confirmation that the electronic quantum well behaviour is still intact, the effect of the perforation of the quantum well was investigated. Figure 4.6a and b show typical images of the perforated quantum well, the periodicity of the pores is 41 nm. The periodicity is determine by a line profile as can be observed in the inset of figure 4.6a. The dI/dV spectroscopy measurements were too unstable to obtain conclusive results from. This can be caused by the fact that a small area on the sample was perforated. It took a few hours to a few days to find this area and it is likely that the tip degraded during the searching period. This resulted in a tip that was too unstable to perform spectroscopy measurements.
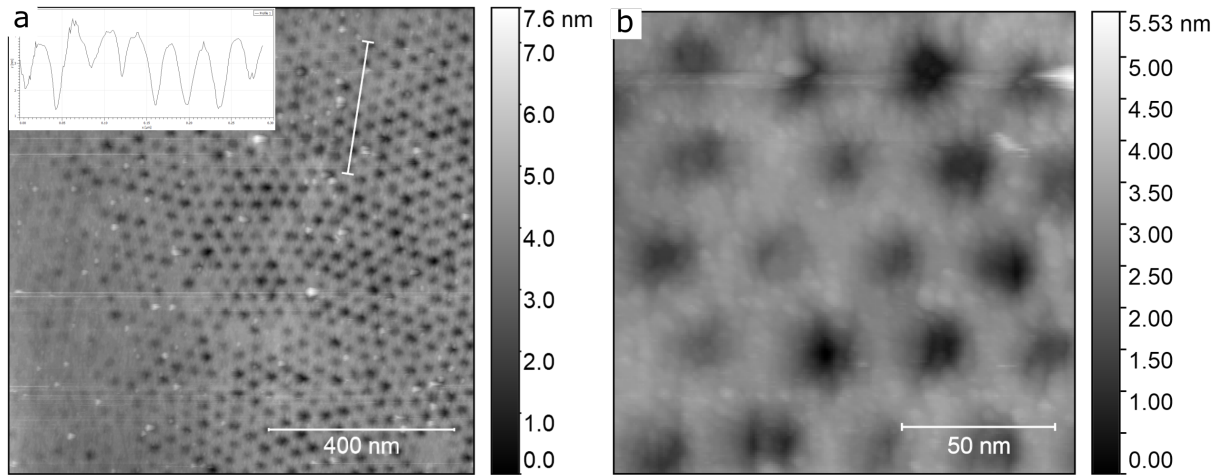
Figure 4.6: a) A typical image of the perforated part of the quantum well on the EBL sample. b) A zoom-in on the perforated quantum well.

4.2.4 Block Co-Polymer Lithography

Figure 4.7a and b show a typical images of the perforated quantum well. The periodicity of the pores is determined by the lineprofile that is shown in the inset of figure 4.7a. A periodicity of 37 nm is determined. In the overview image of the perforated quantum well, many white specks can be observed. These specks are likely remnants of the arsenic layer that was removed by annealing. It can also be observed that there are many orientations present, the long range periodicity is not present. This is caused by the fact that the geometry is obtained by the self assembly of the polymers. Figure 4.8a shows spectra of the atomic site and bridge site. The spectra clearly show different features. The spectrum of the atomic site shows a gradual onset of the first step followed by a steeper increase towards the second step. Contrastingly to the spectrum of the atomic site, the spectrum of the bridge site shows a sharp onset of the first and second peak. The onset of the first step of the atomic site also seems shifted towards higher energies, as well as the onset of the second step. This suggests that the quantum well at the atomic site has a slightly smaller thickness than at the bridge site. The peaks on the first step in the spectrum of the atomic site are barely visible and no peaks are visible on the second step. The peaks in the spectrum of the bridge site are more clearly visible. Therefore the spectrum of the bridge site will first be discussed. The peaks are numbered 1 to 7, the values peak position are given in table 4.1.

Table 4.1: The values for the positions of the peaks in the experimental dI/dV spectrum and calculated LDOS of the bridge site

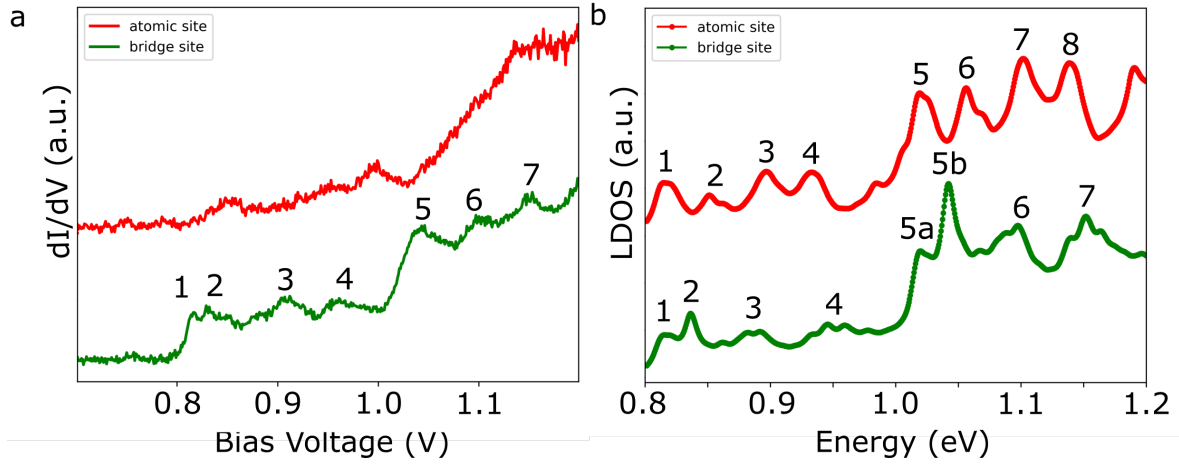| Peak #	1	2	3	4	5	6	7
Peak Position (V)(Experimental)	0.82	0.84	0.91	0.96	1.04	1.1	1.15
Peak Position (eV)(Muffin Tin)	0.82	0.84	0.89	0.95	1.02 (a) 1.05 (b)	1.1	1.16

28

Figure 4.7: a) A typical image of the perforated part of the quantum well on the BCP sample. b) A zoom-in on the perforated quantum well.

Due to the sharp onset of the second step also peaks on the second step can be observed. Peaks 1, 2, 3 and 4 on the first step seem to be repeated on the second step as peak 5, 6 and 7. Although the first step shows three peaks and the second step shows four peaks. Peak 5 on the second step likely consists of 2 peaks that results from peaks 1 and 2 of the first step that are repeated on the second step.

Figure 4.8b shows the calculated LDOS spectra at the atomic site and bridge site from a three dimensional muffin tin calculation. A muffin tin calculation is comparable to solving the Schrödinger equation for a one dimensional potential well between two potential barriers, also known as a particle in a box. However, instead of a single potential well in one dimension, this can be extended to a two dimensional lattice as well as a three dimensional crystal.[54] The pores are then expressed as a potential barrier. By solving the Schrödinger equation for the crystal, the electronic structure can be determined. It should be noted that the muffin tin calculations are with perfectly sized, spaced and circular pores and therefore give results for a perfect system A significant difference is the sharpness of peak 2, which is present in the calculated spectra of the bridge site but not at the atomic site. This peak is likely to be the flat band and is clearly located on the bridge site. Peak 1 of the spectrum of the atomic site is the S band and seems to be split in two peaks. For the muffin tin calculations a peak broadening is chosen, if the broadening is lowered significantly, this peak indeed splits into two peaks. This shows that it is the S band with the Dirac cone. It also seems that the S band is extending in the bridge site accounting for the intensity of peak 1 in the bridge site. Peak 2 in the calculated spectrum of the atomic site seems to consist of two peaks, which is possibly the P band with the Dirac cone. Higher order bands are also present, but are not clearly distinguishable and will therefore not be discussed.

As was observed in the experimental spectrum of the bridge site, the muffin tin calculations also show a repetition in peaks for the atomic site as well as the bridge site. Corresponding features of the first and second step are peaks 1 and 5a from the S band in the first step and second peak, respectively.

Figure 4.8: a) Experimental dI/dV spectra of the atomic site (red) and bridge site (green). b) Calculated LDOS at the atomic site (red) and bridge site (green) ($m^* = 0.041$ m$_e$, $a = 36$ nm, $r = 10$ nm, $V_0 = 1.0$ eV, $\Gamma = 10$ meV).

Also the peaks of the P flat band, peak 2 and 5b of the first step and second step, respectively. The higher order bands also seem to repeat, with peak 3 corresponding to peak 6 and peak 4 corresponding to peak 7. This repetition is also observed in the calculated spectrum of atomic site. In the spectrum peaks 1 to 4 correspond to peaks 5 to 8, respectively. This suggests that the bands originating from the graphene physics are repeated from every step.

By comparing experimental data with computational data, the experimental data can be more accurately investigated. The shape of the spectrum of the atomic site shows no sharp onset of the first and second step. This might be due to the fact that the first peak, the peak from the S band, is not as sharp as is expected from the calculated spectrum. A possible reason from this is that in the real situation the S band delocalized. This delocalization can be caused by disorganization due to the different orientations of the lattice as well as the inconsistency in the shape and size of the pores as well as the distance between the pores. The peak from the S band therefore lacks intensity resulting in a not well defined onset as suggested by the calculated spectrum. The calculated spectra of the atomic site shows that the onset of the second step is not as sharp as compared to the onset of the second step at the bridge site. This fact, together with the delocalization of the S band explains the gradual onset of the second step as observed in the experimental data. Due to the shift in onset and the lack in intensity of the peaks in the spectrum of the atomic site, it is not possible to accurately compare the spectrum to the calculated spectrum. This is however not the case for the spectrum of the bridge site. Peak 1 in the experimental spectrum is the S band, this is because peak 1 in the experimental spectrum can be linked to peak 1 in the calculated spectrum. Peak 1 in the calculated spectrum splits into two peaks when the broadening factor is decreased significantly, this suggests that it is indeed the S band with the dirac cone. The S band is observed as one peak without a Dirac cone which is likely due to the disorganization of the lattice. Peak 2 in the experimental spectrum is presumably the P flat band. In

the calculated spectrum the P flat band is significantly higher in intensity than the S band, which is not what is observed in experimental spectrum. This can also be explained by the delocalization of the bands. The peaks at higher energies are higher order orbitals and are not possible to be accurately assigned. It is, however, possible to compare the higher order peaks of the experimental data with the computational data. Peak 3 and 4 of the experimental data can be linked to peak 3 and 4 of the calculated spectra. As said earlier, peak 5 of the experimental spectrum likely consists of two peaks, by comparing with the calculated spectrum, it is possible to conclude this is comprised of the S band and P flat band on the second step. The peaks from these two band are individually present in the calculated spectrum. Peaks 6 and 7 of the experimental spectrum can be linked to peaks 6 and 7 of the calculated spectrum. The results of both the experimental and calculated spectra strongly suggest that peak 1 and 2 of the experimental spectra are the S band and P flat band, respectively. They are also strongly suggest that the peaks originating from the graphene physics are repeated for every step originating from the quantum well.

Chapter 5

Conclusion and Outlook

5.1 Conclusion

In this thesis, the graphene physics in a two dimensional semiconductor superlattice with honeycomb geometry was investigated. Two different techniques have been used to investigate this: epitaxially attached PbSe quantum dots and a patterned InGaAs quantum well. To investigate the graphene physics, STM and STS measurements were performed. Prior to performing STM measurements on the quantum dot superlattice, AFM measurements were performed to investigate the presence of organic ligand and solvent molecules. The AFM topography images appeared stable, however, STM and STS measurements proved challenging. Topography images were obtained, it was however not possible to perform reliable STS measurements.

The other system was a patterned InGaAs quantum well with a thickness of 10 nm. The quantum well is modified with a triangular pattern of chemically etched pores. Two different sample were produced with two different lithography techniques. The first sample was produced by electron beam lithography and resulted in a periodicity of 41 nm. The second sample was produced by block co-polymer lithography and resulted in a periodicity of 37 nm. The spectra of both sample show steps in the conduction band, thereby confirming that the quantum well behaviour remained intact after perforation. The band gaps of both patterned quantum wells were increased as compared to the the quantum well before patterning. The increase is likely caused by a decrease in thickness after etching of the pores as well as an increase in "dead" quantum well, this results in a decrease in thickness and therefore an increase in the band gap. The sample produced by block co-polymer lithography has a smaller increase in the band gap compared to the sample produced by electron beam lithography, the difference between these samples was the annealing procedure that was performed to remove the arsenic layer. The EBL sample was annealed at higher temperature which likely caused the beryllium dopants in the InP barrier material to have migrated to the InGaAs quantum well. This potentially increased the thickness of the "dead" quantum well, thereby decreasing the thickness of the contributing quantum well. The diminished effective thickness accounts for the increased band gap.

After confirmation that the quantum well was intact, the electron structures at the high symmetry points were investigated. The STS measurements on the EBL sample did not result in conclusive data. This might be due to the sample or due to the tip. The STS measurements on the BCPL sample did result in conclusive data and a clear difference was observed in the electron structure of the atomic site compared to the bridge site. The dI/dV spectra show an onset of the first and second step at higher energies for the atomic site than for the bridge site, this suggests that the thickness of the quantum well is smaller at the atomic site. The peaks of the S band and P flat band was identified in the spectrum of the bridge site by comparison with computational data. It was also experimentally and computationally observed that the peaks in the LDOS originating from the honeycomb geometry are repeated on the steps originating from the quantum well.

5.2   Outlook

However promising the results seem, there is still no concrete experimental evidence for the existence of the Dirac cone in a two-dimensional semiconductor nanostructure. To obtain better measurements there are a number of improvements that can be made. more in depth research can be performed towards the ligand removal of the quantum dot superlattice. If a superlattice without the presence of ligands can be achieved, than the chance of obtaining stable measurements will increase significantly. Following the ligand removal, reliable cation exchange has to be performed. Since the quantum dot superlattice is produced with PbSe quantum dots and the Dirac cones are better defined in a superlattice of CdSe. Other than the ligands and cation exchange, there are not other obstacles for the fundamental investigation of the Dirac cone in the quantum dot superlattice, because lattices have been produced which extend for several hundreds of nanometers. For application purposes, the superlattice should extend several millimeters. To achieve the size for application purposes, more research has to be performed.

The lithography sample can also be improved upon. The width of the Dirac cone is shown to be dependent on the effective mass and the periodicity.[49] By using a material with a lower effective mass, the width of the Dirac cone can be increased. Suitable materials would be InAs or InSb, both having a smaller effective mass than InGaAs. Another improvement would be decreasing the periodicity. This would increase the width of the Dirac cone. The self assembly of the block co-polymer can also be improved upon. If the polymer can self assemble into a more ordered structure in which the pores are evenly spaced, a lattice can be obtained that is more ordered. This increased ordering will translate into clearer features in the dI/dV spectra.

Chapter 6

Acknowledgements

The last, but not the least, part of this thesis are the acknowledgements. In this part I want to thank all the people that have helped me during this almost 1.5 year project.

First I want to thank **Dr. Ingmar Swart** for allowing me, once again, to do a research project in his group. He directed me to Christiaan for my bachelor project which resulted in me also doing my master project under his supervision. I also want to thank him for the interesting discussions and always being willing to help when there is someone in need of help. Although he is a very busy man, its nice to see that he still comes to the basement and really wants to be involved in the research.

Then I want to thank **Christiaan Post** for supervising my master project. When my bachelor project came to an and we kept in touch about a possible master project at CMI, which was possible. I enjoyed your supervision, for both my bachelor and master project, tremendously. Although my initial research goal was not achieved, I could join you with your research. This was really nice, because it was trying to achieve the same thing, but from a very different approach. I will always remember the awfully, amazing music during spectra what kept us motivated to keep on going. There have also been plenty of things outside of research that were really nice. Playing Sinterklaas and Zwarte Piet together with Jos was a really fun experience. Playing pool a couple of times together with Jesper. Making a drunken promise of making your famous mushroom risotto and actually living up to your promise. Many thanks for the past 1 and 3/4 of a year.

I also want to thank **Pierre Capiod**. He helped me during the STM measurements on the quantum dot superlattices. Although the samples were still not clean enough to be measured, it was still a nice time. The hours long Skyrim or Shire music playlists were very soothing.

Another person I want to thank in particular is **Jos Mulkens**, for without him the master would have been much more difficult. The "Modelling and Simulation" course was quite the challenge, even more when also following "Photon Physics". But luckily Jos and I could work together during ModSim and that resulted in him helping me a lot. We were a good team, he helped me with the coding and I made sure that we didn't get sidetracked too much, such that we would get our work finished in time.

Many thanks also to the master students (**Jeroen**, **Rian**, **Jan**, **Nicolette**, **Philipp**, **Arend**, **Kelly**, **Katarina**, **Dirk-Floris**) who have my time at CMI a lot more fun. The nice dinners and drinks we got

as well as the, sometimes too many, conversations when we didn't feel like working.

Another group of people can't miss from my acknowledgements, and they are of course team Basement. **Saoirsé**, **Jesper**, **Marlou**, **Pacal**, **Real Thomas** and all those who have come and gone, thank you very much for the nice group meetings and table football matches.

Also many thanks to the technical staff, **Peter** and **Stephan**, for all the help with the STM and computer.

Lastly, I want to thank the whole of CMI for making it a really nice place to do a research project. The borrels with pizza, gamenights, Sinterklaas, Christmas dinners, group outings and whatnot. I had a really great time!

Chapter 7

Bibliography

[1] Andrey N. Enyashin and Alexander L. Ivanovskii. Graphene allotropes. *Phys. Status Solidi B*, 248(8):1879–1883, January 2011.

[2] Marco Polini, Francisco Guinea, Maciej Lewenstein, Hari C. Manoharan, and Vittorio Pellegrini. Artificial honeycomb lattices for electrons, atoms and photons. *Nature Nanotechnology*, 8(9):625–633, September 2013.

[3] C. Delerue and D. Vanmaekelbergh. Electronic band structure of zinc blende CdSe and rock salt PbSe semiconductors with silicene-type honeycomb geometry. *2D Materials*, 2(3):034008, June 2015.

[4] Kenjiro K. Gomes, Warren Mar, Wonhee Ko, Francisco Guinea, and Hari C. Manoharan. Designer Dirac fermions and topological phases in molecular graphene. *Nature*, 483(7389):306–310, March 2012.

[5] E. Kalesaki, W. H. Evers, G. Allan, D. Vanmaekelbergh, and C. Delerue. Electronic structure of atomically coherent square semiconductor superlattices with dimensionality below two. *Phys. Rev. B*, 88:115431, Sep 2013.

[6] C. de Mello Donega, editor. *Nanoparticles: Workhorses of Nanoscience*. Springer, 2014.

[7] C. Kittel. *Introduction to Solid State Physics*. John Wiley & Sons, 2005.

[8] F. Bloch. Über die Quantenmechanik der Elektronen in Kristallgittern. *Zeitschrift für Physik*, 52(7):555–600, July 1929.

[9] Wahyu Setyawan and Stefano Curtarolo. High-throughput electronic band structure calculations: Challenges and tools. *Computational Materials Science*, 49(2):299–312, August 2010.

[10] A. Abbassi, Zakaryaa Zarhri, Ch Azahaf, Hamid Ez-Zahraouy, and Abdelilah Benyoussef. Boltzmann equations and ab initio calculations: comparative study of cubic and wurtzite CdSe. *SpringerPlus*, 4:543, September 2015.

[11] E. Groeneveld. *Synthesis and Optical Spectroscopy of (Hetero)-Nanocrystals - An exciting interplay between chemistry and Physics*. PhD thesis, Utrecht University, 2012.

[12] R. Koole. *Fundamental and Applications of Semiconductor Nanocrystals*. PhD thesis, Utrecht University, 2008.

[13] A. J. Houtepen. *Charge injection and transport in quantum confined and disordered systems*. PhD thesis, Utrecht University, 2007.

[14] Ithurria, S. and Tessier, M. D. and Mahler, B. and Lobo, R. P. S. M. and Dubertret, B. and Efros, Al. L. Colloidal nanoplatelets with two-dimensional electronic structure. *Nature Materials*, 10(12):936–941, December 2011.

[15] H. E. Hall J. R. Hook. *Solid State Physics*. John Wiley And Sons Ltd, 1991.

[16] Juan Jimenez, Jens W. Tomm, Juan Jimenez, and Jens W. Tomm. Introduction. In *Spectroscopic Analysis of Optoelectronic Semiconductors*, pages 1–48. Springer International Publishing, Cham, 2016.

[17] M. W. Prairie and R. M. Kolbas. A general derivation of the density of states function for quantum wells and superlattices. *Superlattices and Microstructures*, 7(4):269 – 277, 1990.

[18] E. Kalesaki, C. Delerue, C. Morais Smith, W. Beugeling, G. Allan, and D. Vanmaekelbergh. Dirac Cones, Topological Edge States, and Nontrivial Flat Bands in Two-Dimensional Semiconductors with a Honeycomb Nanogeometry. *Phys. Rev. X*, 4:011010, Jan 2014.

[19] A. Tadjine, G. Allan, and C. Delerue. From lattice Hamiltonians to tunable band structures by lithographic design. *Phys. Rev. B*, 94:075441, Aug 2016.

[20] K. Cho, D. V. Talapin, W. Gaschler, and C. B. Murray. Designing PbSe Nanowires and Nanorings through Oriented Attachment of Nanoparticles. *J. Am. Chem. Soc.*, 127(19):7140–7147, May 2005.

[21] J. Polleux, N. Pinna, M. Antonietti, and M. Niederberger. Ligand-Directed Assembly of Preformed Titania Nanocrystals into Highly Anisotropic Nanostructures. *Adv. Mater.*, 16(5):436–439, December 2004.

[22] N. Castro, C. Bouet, S. Ithurria, N. Lequeux, D. Constantin, P. Levitz, D. Pontoni, and B. Abécassis. Insights into the Formation Mechanism of CdSe Nanoplatelets Using in Situ X-ray Scattering. *Nano Lett.*, 19(9):6466–6474, September 2019.

[23] C. Schliehe, B. H. Juarez, M. Pelletier, S. Jander, D. Greshnykh, M. Nagel, A. Meyer, S. Foerster, A. Kornowski, C. Klinke, and H. Weller. Ultrathin PbS Sheets by Two-Dimensional Oriented Attachment. *Science*, 329(5991):550, July 2010.

[24] C. S. S. Sandeep, J. M. Azpiroz, W. H. Evers, S. C. Boehme, I. Moreels, S. Kinge, L. D. A. Siebbeles, I. Infante, and A. J. Houtepen. Epitaxially Connected PbSe Quantum-Dot Films: Controlled Neck Formation and Optoelectronic Properties. *ACS Nano*, 8(11):11499–11511, November 2014.

[25] W. H. Evers, B. Goris, S. Bals, M. Casavola, J. de Graaf, R. van Roij, M. Dijkstra, and D. Vanmaekelbergh. Low-Dimensional Semiconductor Superlattices Formed by Geometric Control over Nanocrystal Attachment. *Nano Lett.*, 13(6):2317–2323, June 2013.

[26] M. P. Boneschanscher, W. H. Evers, J. J. Geuchies, T. Altantzis, B. Goris, F. T. Rabouw, S. A. P. van Rossum, H. S. J. van der Zant, L. D. A. Siebbeles, G. Van Tendeloo, I. Swart, J. Hilhorst, A. V. Petukhov, S. Bals, and D. Vanmaekelbergh. Long-range orientation and atomic attachment of nanocrystals in 2D honeycomb superlattices. *Science*, 344(6190):1377, June 2014.

[27] J. J. Geuchies, C. van Overbeek, W. H. Evers, B. Goris, A. de Backer, A. P. Gantapara, F. T. Rabouw, J. Hilhorst, J. L. Peters, O. Konovalov, A. V. Petukhov, M. Dijkstra, L. D. A. Siebbeles, S. van Aert, S. Bals, and D. Vanmaekelbergh. In situ study of the formation mechanism of two-dimensional superlattices from PbSe nanocrystals. *Nature Materials*, 15(12):1248–1254, December 2016.

[28] J. Vos. Synthesis and TEM investigation of PbSe and CdSe nanocrystals and nanocrystal superlattices. Master's thesis, Condensed Matter and Interfaces, Utrecht University, 2017.

[29] ShinEtsu MicroSi. The Difference Between Positive and Negative Photoresist, March 2013.

[30] M. Park, C. Harrison, P. M. Chaikin, R. A. Register, and D. H. Adamson. Block Copolymer Lithography: Periodic Arrays of 10<sup>11</sup> Holes in 1 Square Centimeter. *Science*, 276(5317):1401, May 1997.

[31] R. Tiron, A. Gharbi, M. Argoud, X. Chevalier, J. Belledent, P. Pimmenta Barros, I. Servin, C. Navarro, G. Cunge, S. Barnola, L. Pain, M. Asai, and C. Pieczulewski. The potential of block copolymer's directed self-assembly for contact hole shrink and contact multiplication. In William M. Tong, editor, *Alternative Lithographic Technologies V*, volume 8680, pages 191 – 201. International Society for Optics and Photonics, SPIE, 2013.

[32] K. Aissou, J. Shaver, G. Fleury, G. Pécastaings, C. Brochon, C. Navarro, S. Grauby, J. M. Rampnoux, S. Dilhaire, and G. Hadziioannou. Nanoscale Block Copolymer Ordering Induced by Visible Interferometric Micropatterning: A Route towards Large Scale Block Copolymer 2D Crystals. *Adv. Mater.*, 25(2):213–217, November 2013.

[33] Oxford Instruments. The Difference Between Positive and Negative Photoresist, 2019. visited on 12-12-2019.

[34] H. Jansen, H. Gardeniers, M. de Boer, M. Elwenspoek, and J. Fluitman. A survey on the reactive ion etching of silicon in microtechnology. *Journal of Micromechanics and Microengineering*, 6(1):14–28, March 1996.

[35] R. Reifenberger. *Fundamentals of Atomic Force Microscopy—Part I: Foundations*, volume 41. Cambridge University Press, 2016.

[36] L. C. Post. An Ambient Atomic Force Microscopy Study on the Coverage of Semiconductor Colloidal Nanoplatelets on Highly Oriented Pyrolytic Graphite. Master's thesis, Condensed Matter and Interfaces, Utrecht University, 2015.

[37] Y. F. Dufrêne. Atomic Force Microscopy, a Powerful Tool in Microbiology. *American Society for Microbiology Journals*, 184(19):5205–5213, October 2002.

[38] H. Oza. How does atomic force microscopy work? - Quora, 2018. https://www.quora.com/How-does-atomic-force-microscopy-work/ visited on 12-12-2019.

[39] Y. F. Dufrêne, T. Ando, R. Garcia, D. Alsteens, D. Martinez-Martin, A. Engel, C. Gerber, and D. J. Müller. Imaging modes of atomic force microscopy for application in molecular and cell biology. *Nature Nanotechnology*, 12(4):295–307, April 2017.

[40] Y. Gan. Atomic and subnanometer resolution in ambient conditions by atomic force microscopy. *Surface Science Reports*, 64(3):99 – 121, 2009.

[41] H. J. Shih and P. J. Shih. Tip Effect of the Tapping Mode of Atomic Force Microscope in Viscous Fluid Environments. *Sensors*, 15(8), 2015.

[42] C. J. Chen. *Introduction to Scanning Tunneling Microscopy*. Oxford University Press, 1993.

[43] G. Binnig, H. Rohrer, Ch. Gerber, and E. Weibel. Tunneling through a controllable vacuum gap. *Applied Physics Letters*, 40(2):178–180, 1982.

[44] J. Tersoff and D. R. Hamann. Theory of the scanning tunneling microscope. *Phys. Rev. B*, 31:805–813, Jan 1985.

[45] M. R. Slot. *Patterning atomic flatland: Electronic lattices crafted atom by atom.* PhD thesis, Utrecht University, 2019.

[46] N. Marturi. *Vision and Visual Servoing for Nanomanipulation and Nanocharacterization using Scanning Electron Microscope.* PhD thesis, University of Franche-Comté, 2013.

[47] J. L. Peters, T. Altantzis, I. Lobato, M. Alimoradi Jazi, C. van Overbeek, S. Bals, D. Vanmaekelbergh, and S. Buhbut Sinai. Mono- and Multilayer Silicene-Type Honeycomb Lattices by Oriented Attachment of PbSe Nanocrystals: Synthesis, Structural Characterization, and Analysis of the Disorder. *Chemistry of Materials*, 30(14):4831–4837, 2018.

[48] Raúl J. Martín-Palma, Akhlesh Lakhtakia, Akhlesh Lakhtakia, and Raúl J. Martín-Palma. *Chapter 15 - Vapor-Deposition Techniques.* Elsevier, Boston, January 2013.

[49] L. C. Post, T. Xu, N. A. Franchina Vergel, A. Tadjine, Y. Lambert, F. Vaurette, D. Yarekha, L. Desplanque, D. Stiévenard, X. Wallart, B. Grandidier, C. Delerue, and D. Vanmaekelbergh. Triangular nanoperforation and band engineering of InGaAs quantum wells: a lithographic route toward Dirac cones in III–V semiconductors. *Nanotechnology*, 30(15):155301, February 2019.

[50] M. Tahir and U. Schwingenschlögl. Valley polarized quantum Hall effect and topological insulator phase transitions in silicene. *Scientific Reports*, 3(1):1075, January 2013.

[51] N. A. Franchina Vergel, A. Tadjine, V. Notot, M. Mohr, A. Kouassi N'Guissan, C. Coinon, M. Berthe, L. Biadala, K. K. Sossoe, M. M. Dzagli, J.-C. Girard, G. Rodary, L. Desplanque, R. Berndt, D. Stiévenard, X. Wallart, C. Delerue, and B. Grandidier. Influence of doping level and surface states in tunneling spectroscopy of an $In_{0.53}Ga_{0.47}As$ quantum well grown on p-type doped InP(001). *Phys. Rev. Materials*, 3:094604, Sep 2019.

[52] E. V. Ubyĭvovk, D. K. Loginov, I. Ya. Gerlovin, Yu. K. Dolgikh, Yu. P. Efimov, S. A. Eliseev, V. V. Petrov, O. F. Vyvenko, A. A. Sitnikova, and D. A. Kirilenko. Experimental determination of dead layer thickness for excitons in a wide GaAs/AlGaAs quantum well. *Physics of the Solid State*, 51(9):1929–1934, Sep 2009.

[53] B. E. Maile, A. Forchel, R. Germann, and D. Grützmacher. Impact of sidewall recombination on the quantum efficiency of dry etched InGaAs/InP semiconductor wires. *Applied Physics Letters*, 54(16):1552–1554, 1989.

[54] O. K. Andersen and R. G. Woolley. Muffin-tin orbitals and molecular calculations: General formalism. *Molecular Physics*, 26(4):905–927, October 1973.